AGU PUBLICATIONS

Geochemistry, Geophysics, Geosystems

RESEARCH ARTICLE
10.1002/2017GC006908

Geochemical and geophysical constrains on the dynamic topography of the Southern African Plateau

Alan G. Jones[1,2,3], Juan Carlos Afonso[2,4], and Javier Fullea[3]

[1]Complete MT Solutions Inc., Ottawa, Ontario, Canada, [2]Department of Earth and Planetary Sciences, Macquarie University, Sydney, New South Wales, Australia, [3]Dublin Institute for Advanced Studies, Dublin, Ireland, [4]Centre for Earth Evolution and Dynamics, University of Oslo, Oslo, Norway

Key Points:
- Joint stochastic inversion of four distinct geophysical data types for Kaapvaal Craton
- Geochemical, thermal, and water content constraints applied in final test
- Infers that there is dynamic support of the order of 650 m

Supporting Information:
- Supporting Information S1

Correspondence to:
A. G. Jones,
alan.jones.geophysics@gmail.com

Citation:
Jones, A. G., J. C. Afonso, and J. Fullea (2017), Geochemical and geophysical constrains on the dynamic topography of the Southern African Plateau, *Geochem. Geophys. Geosyst.*, *18*, 3556–3575, doi:10.1002/2017GC006908.

Received 2 MAR 2017
Accepted 28 JUL 2017
Accepted article online 14 AUG 2017
Published online 5 OCT 2017

Abstract The deep mantle African Superswell is considered to contribute to the topographic uplift of the Southern African Plateau, but dynamic support estimates vary wildly depending on the approach and data used. One reason for these large disparities is that the role of lithospheric structure, key in modulating deep dynamic contributions to elevation, is commonly ignored or oversimplified in convection studies. We use multiple high-quality geophysical data coupled with xenolith-based geochemical constraints to compute the isostatic lithospheric contribution to the elevation of the Plateau, facilitating isolation of the current dynamic component from the total observed elevation. We employ a multiobservable stochastic algorithm to invert geoid anomaly, surface-wave dispersion data, magnetotelluric data, and surface heat flow to predict elevation in a fully thermodynamically and internally-consistent manner. We find that a compositionally layered 230 $\pm$ 7 km thick lithosphere is required to simultaneously fit all four data types, in agreement with abundant independent xenolith evidence. Our stochastic modeling indicates a lithospheric contribution to elevation of the order of 670 m, which implies dynamic support arising from the convecting sublithospheric mantle of $\sim$650 m. Our results have important implications for the understanding of lithospheric-deep mantle feedback mechanisms and for calibrating dynamic topography estimates from global convection studies.

Plain Language Summary Is the Kaapvaal Craton too high? Yes is the short answer. Its elevation cannot be sustained by the lithosphere of the craton itself, therefore there must be support from beneath the base of the lithosphere, so-called dynamic topography. We show through very careful modelling of the Kaapvaal Craton lithosphere that alone it can support an elevation of the order of 670 m, therefore the other approx. 650 m must come from mantle processes beneath the base of the lithosphere.

1. Introduction

Dynamic topographic support of elevated plateaus by deep mantle convection is currently a key but highly contentious issue, as it pertains directly to the mechanical coupling between lithospheric plates and convecting mantle as well as to the viscosity structure and lateral density heterogeneity within the deep mantle [cf. *Flament et al*., 2013; *Hoggard et al*., 2016]. *Hager et al*. [1985] were the first to relate global seismic velocity heterogeneity to large-scale density anomalies in the lower mantle, and they inferred a dynamic contribution to topography of >250 m for the whole of Africa in their degree 2–3 model. Partial support of the Southern African Plateau (SAP) by the Southern African Super-Plume has received the greatest attention of the global type examples of dynamic topography. More importantly, southern Africa is a unique, arguably the best, natural laboratory for testing theories given the wealth of extant and available geological, geophysical, and geochemical data.

The formative regional inference of southern African dynamic topography was based on residual bathymetry of the SE Atlantic [*Nyblade and Robinson*, 1994], which exhibits a broad $\sim$500 m high bathymetric swell, suggesting that the adjacent Southern African Plateau is, in part, dynamically supported. However, the issue is highly controversial, with some advocating upper mantle support for all of the topography [*Vinnik et al*., 1996], and others advocating that the lower mantle must play a significant role given that a large-scale, deep mantle, low velocity anomaly beneath the southern African plate is a persistent feature of all global seismic topographic models, however constructed. An early estimate of the dynamic contribution, based on

instantaneous flow models inferred from velocity anomalies at depths >350 km, suggested 450–650 m of dynamic topographic support for the Kaapvaal Craton [*Lithgow-Bertelloni and Silver*, 1998]. Subsequent seismic tomography models showed an extensive low velocity anomaly, interpreted as a thermal anomaly, rising from the core-mantle boundary through the whole mantle beneath the SE Atlantic [*Romanowicz and Gung*, 2002]. Recent work using the Southern African Seismic Array (SASE) data is interpreted as not providing any support for an explanation for the high topography of the Kalahari Craton (Kaapvaal and Zimbabwe Cratons taken together) restricted to the upper mantle only [*Brandt et al*., 2012], although quantitative constraints on the amount of dynamic topography are not provided.

Global geodynamic models of mantle flow, five of which are compared in *Flament et al*. [2013], are all consistent in inferring dynamic support for the Southern African Plateau, but the amount varies between the authors. Four of these are in general agreement suggesting 0–400 m of dynamic topography, whereas one proposes a larger estimate of 800–1200 m. The uplift history of the SAP based on its stratigraphic record is another approach for estimating its dynamic support. The first such study demonstrated consistency with an excess elevation of the order of 450 m and an uplift rate since the Cenozoic to today of 5–20 m/Myr [*Gurnis et al*., 2000]. Using global stratigraphic data and a gravity-topography coherence approach, *Hoggard et al*. [2016] also reported ∼400–500 m for this region

We address the issue of quantifying the amount of dynamic support of the SAP from a novel perspective. We determine quantitatively the isostatic topographic support that can be attributed to the thermochemical structure of the lithosphere, inferring the excess elevation to be the consequence of sublithospheric processes. However, in contrast to the approach of *Brandt et al*. [2012] and of others that are driven primarily by consideration of only seismological data, we perform a joint thermochemical inversion of the geoid anomaly, Rayleigh wave dispersion data, magnetotelluric (MT) data and surface heat flow data, using a self-adaptive Markov Chain Monte Carlo algorithm, within a thermodynamically and internally consistent framework [*Afonso et al*., 2013a, 2013b, 2016b]. Our inversions take advantage of the wealth and quality of information that exists on the crustal structure, the chemistry and thermal structure of the lithospheric mantle, and the likely lithospheric thickness in southern Africa. In contrast to most studies based on mantle flow simulations, our approach is independent of stringent (and poorly known) assumptions with regard to viscosity structure and conversions of velocity anomalies into density anomalies in the deep mantle, but makes use of well-understood geophysical theories only [*Afonso et al*., 2008, 2013a, 2013b, 2016b]. Moreover, the complementary nature of the data sets imposes stricter constraints on our models, in a similar manner to those of *Steinberger* [2016] and *Colli et al*. [2016].

2. Stochastic Modeling Method

The integrated multiobservable modeling approach used here is described in detail in *Afonso et al*. [2008, 2013a, 2013b]. The adaptive Markov Chain Monte Carlo inversion scheme is based on the DRAM algorithm of *Haario et al*. [2006] and is described in *Afonso et al*. [2016a]. We compute stable mineral assemblages in the mantle and all their relevant bulk properties (density, elastic moduli, electrical conductivity, etc.) as function of chemical (major-element) composition, pressure, and temperature by Gibbs free-energy minimization. All calculations were performed in the system CaO, FeO, MgO, Al_2O_3, and SiO_2 (CFMAS) using the database and formalism of *Stixrude and Lithgow-Bertelloni* [2011] and components of the software Perple_X [*Connolly*, 2009]. The a priori compositional information is based on a global database of mantle rocks that covers most of the natural variability observed in mantle samples, as discussed in *Afonso et al*. [2013a, 2013b]. We perform these calculations assuming a one-dimensional (1-D) subsurface, i.e., that there is little lateral variation in physical parameters for distances greater than the depth of penetration. The validity of this assumption is demonstrated particularly in the MT data.

3. Data and Constraints

3.1. Regional Average Elevation

We seek to determine the elevation that can be isostatically supported by a lithosphere structure that consistently explains other observations, hence the regional average elevation is not a datum per se, but is information we require to estimate the amount of dynamic support. The topography of southern Africa is shown in Figure 1. The robust average and median regional elevation within 350 km of the Jagersfontein

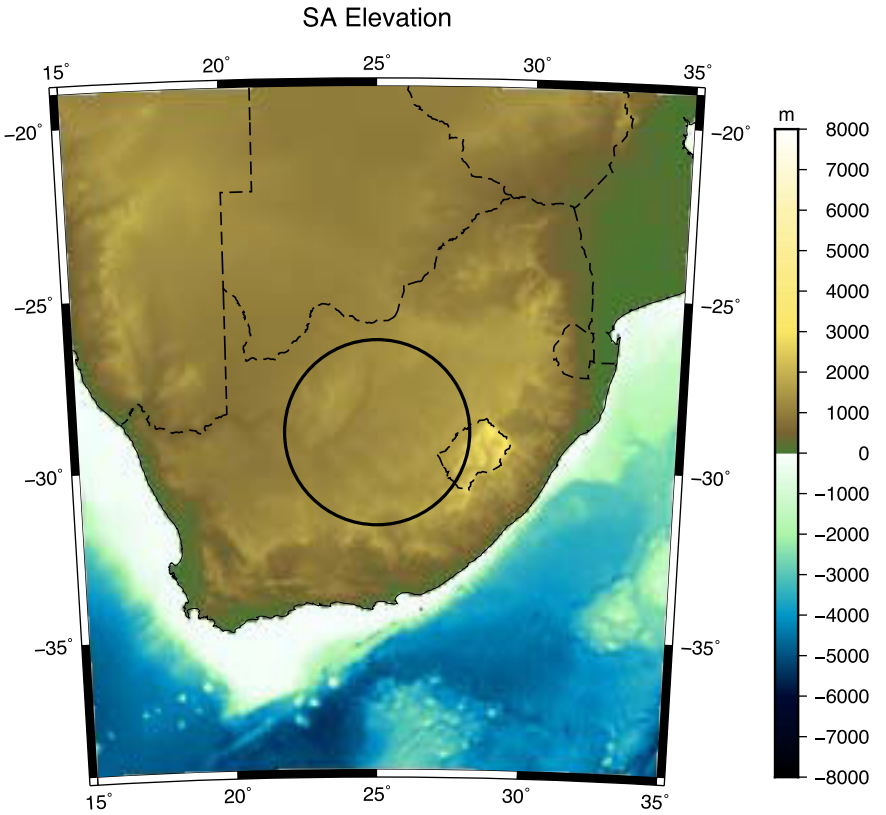

Figure 1. Topography of southern Africa. The circle represents a 350 km radius around the Jagersfontein kimberlite field. Political boundaries are depicted as dashed lines.

kimberlite field at approximately 30°S and 25°E are 1316 m and 1322 m, respectively, with a standard deviation of 177 m, i.e., the region is essentially flat. We thus assume that the regional elevation is of the order of 1320 m.

3.2. Filtered Geoid and Topography

Since all masses within the Earth contribute to all harmonic degrees of the unfiltered EGM2008 geoid model (Figure 2a), a high-pass filter needs to be applied to eliminate the contributions mostly associated with deep density anomalies (e.g., in the lower mantle and CMB) that are not considered in the inversion carried out in this work. Following the general analysis of *Bowin* [2000] and *Afonso* [2006], wavelengths larger than $\sim$2500 km, which can be associated with causative masses at maximum depths $>$450 km, were removed from the full wavelength geoid. We also filter out short wavelengths less than 100 km associated with shallow short-wavelength features in the crust not relevant in this study. This was performed using a passband filter of 200–1600 km, with cosine tapers to 100 km and 2500 km, respectively. The filtered geoid data are plotted in Figure 1b. The mean of the filtered geoid values within 350 km of the location of the MT site is 2 m, with a standard deviation of the distribution of 1 m. This filtered geoid value was used as the input value in the inversions.

3.3. Surface Heat Flow

The Kaapvaal Craton, excluding the areas of the Witwatersrand Basin and the Bushveld igneous complex, is characterized by an E-W variation in surface heat flow (SHF), with values of 38 ± 7 and 53 ± 4 mW m^{-2} in its western and eastern portions, respectively [*Jones*, 1998]. We take the former of those (38 ± 7 mW m^{-2}) as our input SHF data, as the latter is representative of the western Kaapvaal Craton.

3.4. Rayleigh Surface Wave Dispersion Data

The Rayleigh surface wave dispersion data for SW Kaapvaal Craton were provided by Dr. Joanne Adam from *Adam and Lebedev* [2012] and are plotted in Figure 3. These data represent an average along paths in the

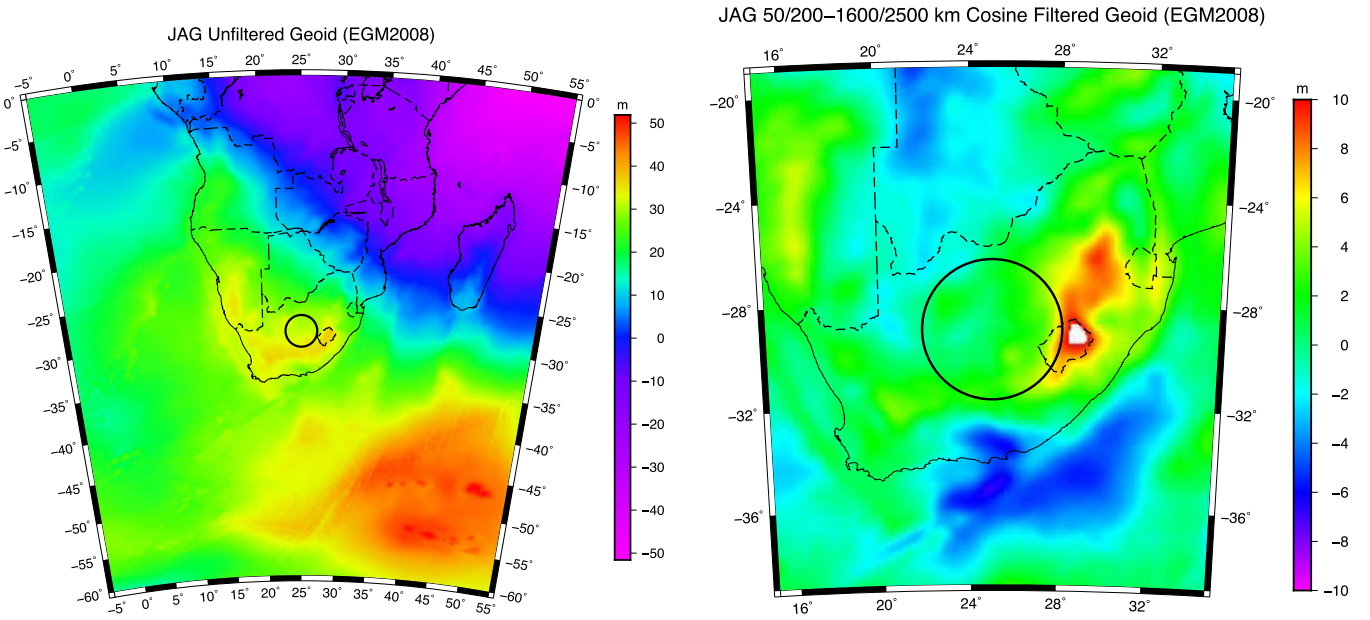

Figure 2. (a, left) Unfiltered regional geoid (from EGM2008). (b, right) Filtered geoid (from EGM2008) removing contributions from both long wavelengths (>2500 km) and short wavelengths (<100 km). The location of the MT site used, which is within the Jagersfontein kimberlite field, is the center of the 350 km averaging circle. Solid faint lines are coastlines, and dashed lines are national boundaries.

SW part of the craton. The full data set comprised estimates at 115 periods from 4.96 to 400.16 s. The estimates at the five longer periods beyond 200 s were excluded, as those penetrate beyond 410 km. The remaining 110 data were decimated by taking one point in every three yielding 34 estimates from 4.96 to 200 s. Error estimates were on average 1.35%, with the best estimates with 1% error at periods of 30–40 s and rising to 1.5% at the shortest period and 2.35% at the longest period.

3.5. Magnetotelluric Data

The magnetotelluric data are those from site KIM015 within the Jagersfontein kimberlite field that were previously modeled in *Fullea et al.* [2011] and discussed in *Jones et al.* [2013]. The full four elements of the MT impedance tensor are shown in Figure 4a. Note that the off-diagonal elements (XY and YX) are close to each other to the very longest periods. (The sharp and unphysical drop off at the three shortest periods/

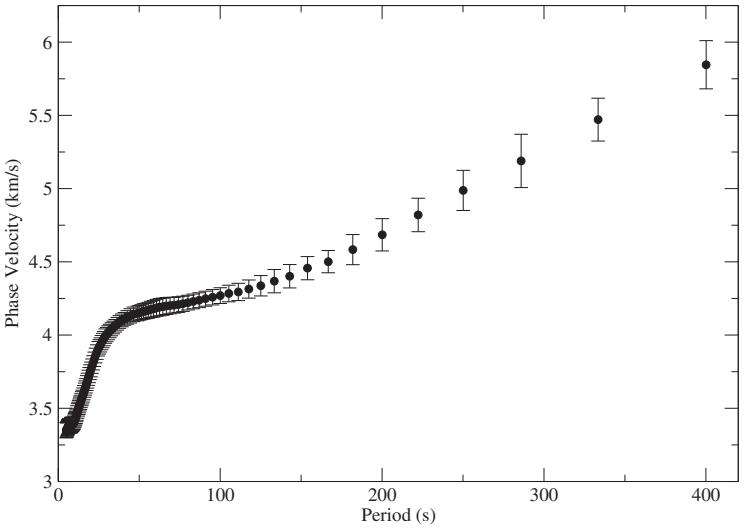

Figure 3. Rayleigh wave dispersion data from *Adam and Lebedev* [2012].

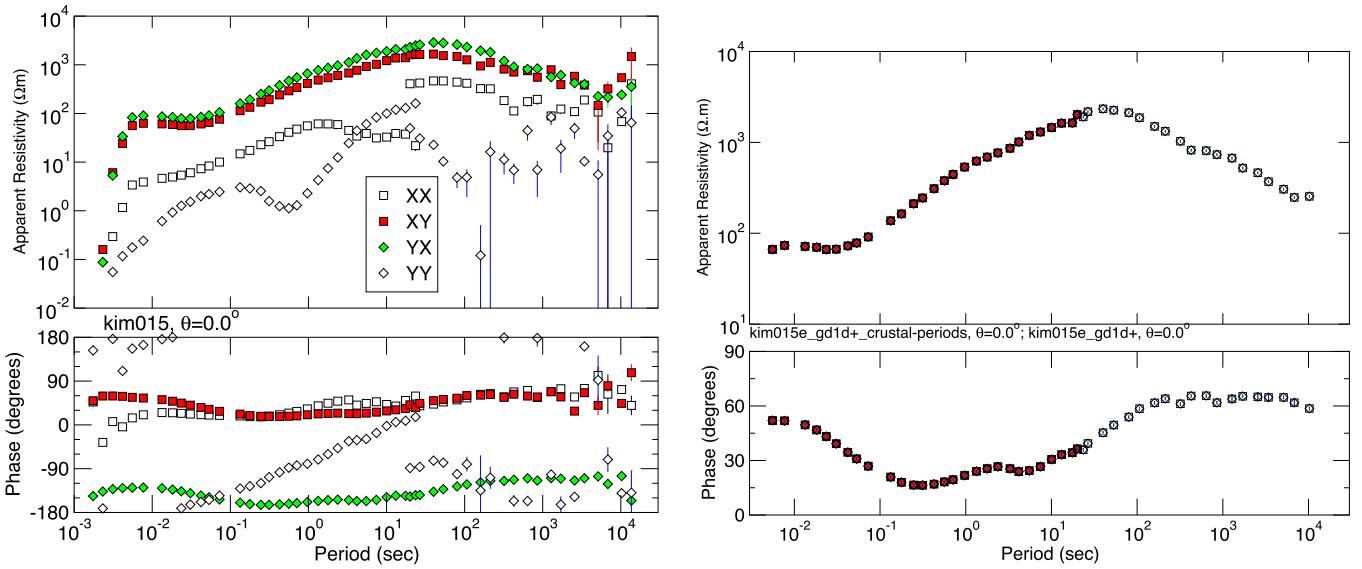

Figure 4. (a, left) MT impedance tensor data for site KIM015 in geographic coordinate system. The off-diagonal elements XY and YX are colored, whereas the diagonal elements are not. (B, right) Distortion and Rho+ corrected 1-D MT data.

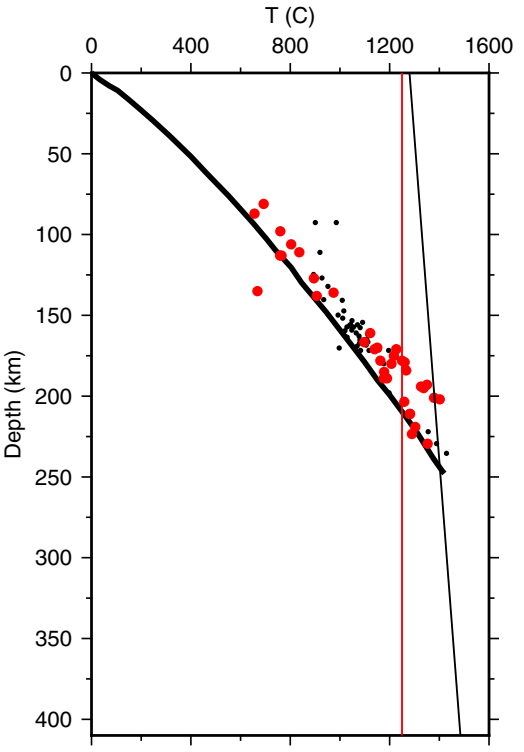

Figure 5. Geotherm K2 (solid black line) of the Kaapvaal Craton derived by *Jones* [1988] based on the heat flow from granitic terranes, and the petrologically derived P-T data based on petrological geothermometry of xenoliths from the Group I kimberlites on the Kaapvaal Craton [*Woodland and Koch*, 2003] (red for Jagersfontein, black for other kimberlite fields). The solid thin black line is the peridotite melting adiabat of *McKenzie and Bickle* [1988, 1990], and the solid thin red line is 1250°C, which is here assumed to correspond to the base of the thermal LAB.

highest frequencies is due to either low quality data or to electrode effects.) The off-diagonal terms are, within errors, identical to one-another, and the diagonal terms are far smaller—these are indicators of the subsurface being one-dimensional, i.e., layered with isotropic conductivity in each layer, for a lateral distance at least as far as the depth of penetration.

The off-diagonal impedance tensor data were averaged (geometric mean of the ZXY and ZYX impedance tensor elements), corrected for local distortion of a regional isotropic 1-D Earth (an isotropic variant of the 1-D anisotropic distortion approach described in *Jones* [2012]), and then tested and corrected for internal compatibility and corrected using Rho+ [*Parker and Booker*, 1996]. The final data are shown in Figure 4b.

Tests were conducted to determine the crustal probing (red points in Figure 4b, periods $<$20 s) and the mantle probing (open symbols in Figure 4b, periods $>$20 s) periods, and a best fitting three-layered model constructed for the crustal probing periods; that model is discussed and listed in Table 2 below in section 3.7. The mantle probing periods were used as the input MT data in the inversions.

3.6. Estimated Geotherms Based on Heat Flow and Xenoliths

Although we invert for present-day temperature structure, we take as indicative for comparison purposes the calculated geotherms beneath the area resulting from two different approaches.

Table 1. Initial Seismic Crustal Structure (From *Muller et al.* [2013]) and Prior Distributions[a]

Layer	Thickness (m)	Vp (km/s)	Vs (km/s)	Vp/Vs	Density (kg/m^3)
Layer 1	12,840 ± 2000	6.232	3.619	1.65–2.00	2800 (2650–2950)
Layer 2	9340 ± 2000	6.598	3.694	1.65–1.83	2850 (2800–3000)
Layer 3	14,690 ± xxx[b]	7.217	4.033	1.65–1.83	2950 (2800–3100)

[a]Total crustal thickness is constrained to be 36.9 ± 1 km. Vp/Vs velocity ratios allowed to fall within the prescribed ranges. Initial densities derived from *Christensen and Mooney* [1995].
[b]The distribution on Layer 3 is varied such that total crustal thickness must lie in the range 36,970 ± 2000 m.

The first is the geotherm K2 for the Kaapvaal Craton determined by *Jones* [1988]. Geotherm K2 is derived excluding data from the Witwatersrand Basin and the Vredefort Dome, and has a somewhat steeper gradient than geotherm K1 derived using those data. K2 intersects the 1300°C potential temperature mantle adiabat at 250 km, whereas K1 intersects the adiabat at 220 km (Figure 11 in *Jones* [1988]). Geotherm K2 is shown as the solid black line in Figure 5.

The second estimate of the geotherm is taken from petrologically-derived geothermobarometry on xenoliths from Group I kimberlites on the Jagersfontein field as well as other kimberlite fields on the Kaapvaal Craton undertaken by *Woodland and Koch* [2003]. Those points are also shown in Figure 5 (red for Jagersfontein, and black for other Kaapvaal Craton xenoliths). The Group I kimberlites are the most recently erupted from the major "bloom" of kimberlites at ca 90 ± 10 Ma and the bloom was preceded by a slow build-up in magmatic activity from ca. 180 Ma.

3.7. Crustal Velocity and Density Structure

The crustal velocity structure of the Kaapvaal Craton is robustly known given the wealth of seismological information that exists [*Nguuri et al.*, 2001; *Stankiewicz et al.*, 2002; *James et al.*, 2003; *Yang et al.*, 2008; *Kgaswane et al.*, 2009; *Youssof et al.*, 2013]. Table 1 lists the initial thicknesses and their ranges, Vp and Vs velocities and permitted range of their ratios, and the initial densities and their permitted ranges, we adopted for each of the three crustal layers [*Muller et al.*, 2013].

3.8. Crustal Electrical Structure

The crustal electrical structure is listed in Table 2 and was determined by fitting the high frequency (short period, <20 s) MT responses at site KIM015. Error estimates are determined through applying a linearized resolution approach based on singular value decomposition [*Jones*, 1982]. Unresolved is ρ_2, the resistivity of the resistive layer; this is common in EM inductive problems-in a conductive-resistive-conductive sandwich typically only the minimum value of the resistive layer can be determined, not the actual value or the maximum value, unless the layer is sufficiently thick [e.g., *Jones*, 1999].

Table 2. Crustal Electrical Structure

Layer	Thickness (m)	ρ (Ωm)
Layer 1	905 (820–999)	80 (76–84)
Layer 2	1547 (220–10,880)	30,000 (30,000–300,000)
Layer 3	Sum to 36,970 ± xxx[a]	2550 (2280–2850)

[a]Moho depth: Varied during inversions such that it is the same as that for the velocity/density crustal layering (see Table 1).

Table 3. Ranges of the Five CFMAS Oxides in the Mantle Based on a Global Xenolith Database as Reported in *Afonso et al.* [2013b][a]

Oxide	Minimum Percentage	Maximum Percentage
Al_2O_3	0.0	5.0
FeO	5.0	13.0
MgO	34.0	52.0
CaO	0.0	4.5
SiO_2	40.0	50.0

[a]The covariation between the five oxides is discussed in *Afonso et al.* [2013b, 2016a].

3.9. Mantle Oxide Ranges

The global database of CFMAS mantle oxides determined from exhumed xenoliths yields bounds on oxide distributions [*Afonso et al.*, 2013a]. These bounds are shown in Table 3. Moreover, not all major oxides are independent; CaO, MgO, and Al_2O_3 in peridotitic rocks are strongly correlated. These correlations are well-known to mantle petrologists and geochemists and are useful in reducing the parameter space during the inversion. *Afonso et al.* [2013a, 2016a] have summarized these observations and their use in the context of probabilistic inversions. We refer the reader to those publications for more details on the sampling strategy.

For the sublithospheric mantle, which is presumed to have a bulk chemistry similar to Primitive Upper

Table 4. Ranges of Oxides for Primitive Upper Mantle

	SiO_2	Al_2O_3	FeO	MgO	CaO
McDonough and Sun [1995]	40.40–49.40	3.99–4.87	7.24–8.84	34.00–41.60	3.18–3.86
Lyubetskaya and Korenaga [2007]	43.71–46.19	2.92–4.12	7.43–8.51	37.97–41.03	2.32–3.26
Combined	40.40–49.40	2.92–4.87	7.24–8.84	34.00–41.60	2.32–3.86

Mantle (PUM), tighter bounds can be imposed. The most common PUM oxide ranges adopted are those given by *McDonough and Sun* [1995]. More recently, *Lyubetskaya and Korenaga* [2007] proposed somewhat different ranges. To allow the greatest flexibility in model selection, these two are combined (Table 4) and the joint bounds are used as the oxide chemistry of the sublithospheric mantle.

In the final test, Test 5, the oxide chemistry bounds of the mantle layers are constrained to fit those observed in Kaapvaal mantle xenoliths, as reported in *Griffin et al*. [2003]. These are listed in Table 5.

4. Tests

A large number of tests (full inversions) were performed of various combinations of data and constraints. Below we present and discuss five of these that represent successive tests of increasing complexity; the complexity of the data, the complexity of the Earth and the complexity of the constraints. These are:

Test 1: Inversion of the Rayleigh wave dispersion data only for a single-layered lithosphere, without imposing any geochemical constraints (unbounded) except for requiring that the oxides follow covariation relationships as shown in the global database intercorrelations by *Afonso et al*. [2013b] (e.g., samples with $Al_2O_3 > 4$ and simultaneously $CaO < 0.3$ are not allowed).
Test 2: Inversion of the Rayleigh wave dispersion data for a single-layered lithosphere, with constrained lithospheric oxide chemistry such that they fall within the bounds observed in the global database (Table 3) and with sublithospheric mantle chemistry as bounded by the ranges in Table 4.
Test 3: Inversion of the Rayleigh wave dispersion data plus the filtered geoid height data and the surface heat flow data for a single-layered lithosphere, with constrained oxide chemistry as in Test 2.
Test 4: Joint inversion of the MT and Rayleigh wave dispersion data plus the filtered geoid height data and the surface heat flow data for a three-layered lithosphere, with constrained oxide chemistry as in Tests 2 and 3.
Test 5: Joint inversion of the MT and Rayleigh wave dispersion data plus the filtered geoid height data and the surface heat flow data for a three layered lithosphere, with constrained oxide chemistry such that for each lithospheric layer they fall within the bounds observed for the generic Kaapvaal Craton geochemical layering with sublithospheric mantle ranges as given in Table 5.

For all posterior PDFs and model plots, the acceptable models are indicated in yellow when the summed normalized RMS (nRMS) was less than one. Red denotes models that are the best 25% of the posterior PDFs retained, and blue denotes models that are the best 5% of the posterior PDFs. Gold denotes models contained in the posterior PDFs that fit all examined data types each individually to an RMS or nRMS less than one.

4.1. Test 1: Inversion of Rayleigh Wave Data Only

A total of 200,000 candidate models were created, with DRAM adaptation of the prior distributions every 50,000 models. The prior distributions of the oxides within the lithosphere and sublithospheric mantle were set to uniform in the range 0–100% (i.e., no constrains to be in any specific compositional range, e.g., peridotitic), but the values for each oxide were still governed by their intercorrelations as defined in *Afonso*

Table 5. Geochemical Oxide Layering of the Three-Layer Mantle Lithosphere and Sublithospheric Mantle (Asthenosphere) Based on *Griffin et al*. [2003]

Layer	Depth to Base (km)	Al_2O_3	FeO	MgO	CaO
Layer 1: Low temperature lherzolite	120 ± 10	1.4 ± 0.05	6.6 ± 0.3	46.5 ± 2.0	0.50 ± 0.05
Layer 2: Harzburgite	160 ± 10	1.3 ± 0.05	6.0 ± 0.3	46.0 ± 2.0	0.50 ± 0.05
Layer 3: High temperature lherzolite	240 ± 60	1.75 ± 0.05	8.1 ± 0.4	44.5 ± 2.0	1.27 ± 0.1
Layer 4: Asthenosphere	410	2.5–4.5	6.0–9.2	34–55	0.45–0.55

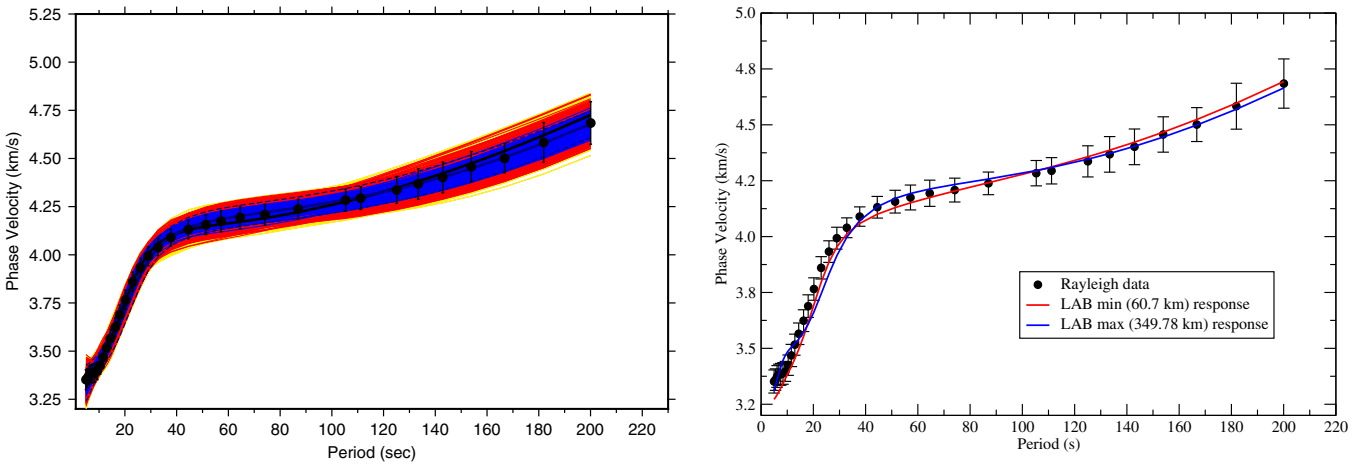

Figure 6. (a, left) Fits of the models to the Rayleigh wave dispersion data for Test 1. Yellow (hidden beneath the red and blue models) denotes models with an nRMS $\leq$ 1, red nRMS $\leq$ 0.93, and blue nRMS $\leq$ 0.60. (b, right): Fits of the two extremal models that fit to nRMS $\leq$ 1 with the minimum LAB (red curve) and the maximum LAB (blue curve) of 60.7 km and 349.78 km, respectively.

et al. [2013b]. The LAB (lithosphere-asthenosphere boundary), here assumed to coincide with the 1250°C isotherm [see *Afonso et al*., 2016a, 2016b, for discussion of this choice], was permitted to vary from 50 to 350 km, with a uniform prior distribution. The crustal velocity and density parameters were allowed to vary as given in Table 1, which is a relatively tight range.

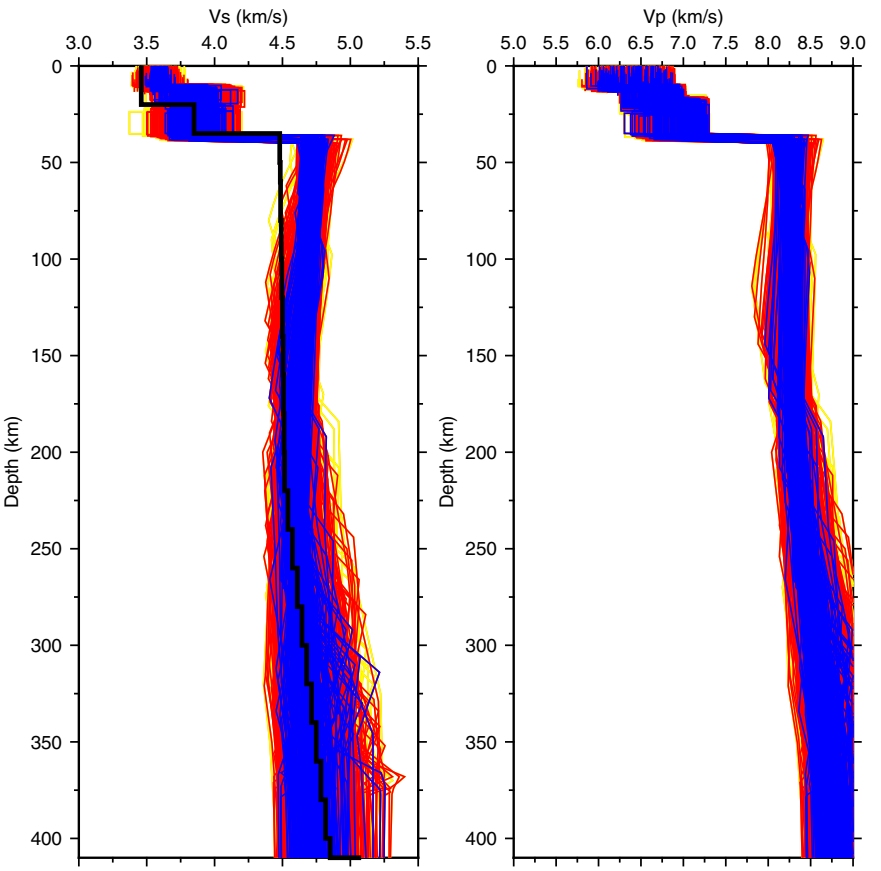

Figure 7. Seismic Vs (left) and Vp (right) models acceptable to the data (Figure 6a) for Test 1. Yellow (hidden beneath the red and blue models) denotes models with an nRMS $\leq$ 1, red nRMS $\leq$ 0.93, and blue nRMS $\leq$ 0.60. Also shown on the Vs models plot is the AK135 global Vs model of *Kennett et al*. [1995].

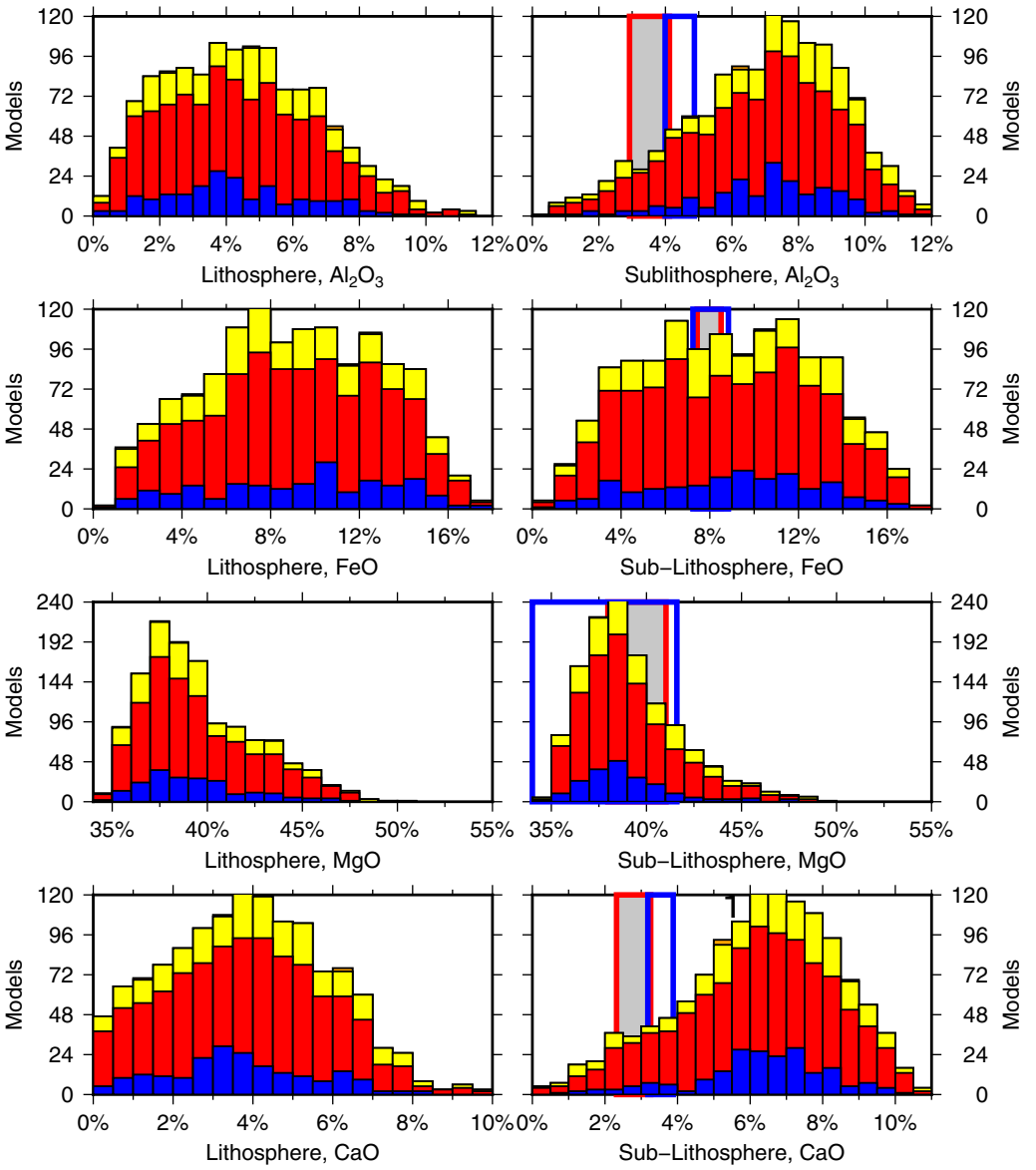

Figure 8. Posterior PDFs of the oxide chemistries of the lithospheric layer (column 1) and the sublithospheric mantle (column 2) for Test 1. The four rows are, respectively, percentages of Al_2O_3, FeO, MgO, and CaO; the fifth oxide, SiO_2, is 100% minus the sum of the other four. The two boxes on the SLM oxides are the Primitive Upper Mantle ranges for *McDonough and Sun* [1995] (blue boxes) and *Lyubetskaya and Korenaga* [2007] (gray shaded red boxes). Yellow denotes models with an nRMS ≤ 1, red nRMS ≤ 0.93, and blue nRMS ≤ 0.60.

The parameter space comprised 29 independent variables, all with defined prior PDFs from which parameters were chosen to create the candidate models. These are described in *Afonso et al*. [2013a], and consist of:

1. One parameter defining the LAB.
2. Four parameters (correlated) for the lithospheric oxides (Al_2O_3, FeO, MgO, and CaO; the fifth one, SiO_2, is not independent as the five must sum to unity).
3. Four parameters (correlated) for the sublithospheric oxides.
4. Six temperature-related parameters.
5. Four parameters defining water content, one in the lithospheric mantle, and three in the three layers of the sublithospheric mantle to 410 km depth. (These parameters are only used when MT data are included.)
6. Three parameters for the density of the crustal layers.
7. Three parameters for the Vp/Vs ratio of the crustal layers.

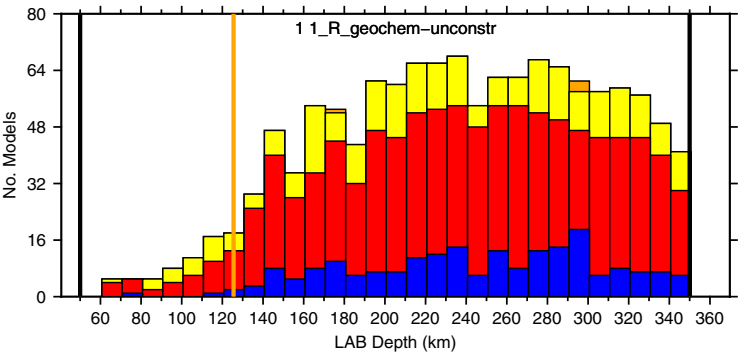

Figure 9. Posterior PDF of the LAB depths corresponding to Test 1. Yellow denotes models with an nRMS $\leq$ 1, red nRMS $\leq$ 0.93, and blue nRMS$\leq$0.60. The thick vertical black lines denote the bounds imposed, and the thick vertical orange line denotes the LAB for the best fitting model.

8. Three parameters related to the permitted interface depths of the crustal layers.
9. One parameter for the mean radioactive heat production of the top two crustal layers.

A total of 4035 models were retained as a sample of the posterior PDFs, of which 1282 had a normalized root mean square (nRMS) of 1.00 or less (indicated in the figures in yellow), 1009 (25% of the total retained) an nRMS $\leq$ 0.93 (red), and 202 (5% of the total retained) an nRMS $\leq$ 0.60 (blue). The fit of the models to the Rayleigh dispersion data is shown in Figure 6a and the fit of the extremal LAB models in Figure 6b. Clearly these models all fit the data acceptably. The seismic Vs and Vp models are shown in Figure 7, and these models look reasonable with Vs velocity in the lithosphere greater than AK135 [*Kennett et al*., 1995] (black line in Figure 7, Vs plot), as expected for a cratonic region.

The oxide posterior distributions for many of these models lie well outside xenolith observed ranges (Figure 8). The LAB posterior distribution (Figure 9) exhibits acceptable solutions for models with an LAB from 60 to 350 km (Figure 6b), the full range of permitted LABs. However, the models with shallow LABs exhibited implausible compositions—the 60 km LAB model has an Al_2O_3 content of 11.2%, an FeO content of 7.2%, an MgO content of 48.1%, a CaO content of 9.8%, and an SiO_2 content of 23.7%. Although the FeO and MgO contents are within the ranges observed globally (Table 3), the others are well outside those ranges, with Al_2O_3 and CaO contents being double the global maximum, and SiO_2 half the global minimum.

These oxide chemistries lead to high Vs and Vp velocities, with Vs up to 4.9 km/s and Vp up to 8.55 km/s in the uppermost lithosphere. Such high Vp velocities have been observed in cratonic regions [e.g., the Siberian craton, *Pavlenkova et al*., 1996], but the highest modeled isotropic Vs velocities in the uppermost mantle are of the order of 4.8 km/s [e.g., western Australia, *Lebedev et al*., 2009]. Given the observed mineral modal percentages for Jagersfontein xenoliths at 100 km of 69.5% olivine, 24.17% orthopyroxene, 3.4% clinopyroxene, and 1.35% garnet, this lherzolite would have a calculated Vs velocity of the order of 4.70–4.73 km/s at the temperature of the Moho (400–500 °C) according to *Jones et al*. [2013].

This illustrates that even with good control on the crustal structure, without other constraints, such as knowledge of acceptable/realistic oxide geochemistry or of likely shear velocities, these Rayleigh wave dispersion data alone, despite being of high quality, are poorly sensitive to the LAB (see Figures 6b and 9).

Finally, the predictions of the elevation, geoid, and SHF from these models are shown in Figure 10. The SHF posterior distribution is reasonable, but the predicted elevations from these models are implausible, and the geoid anomaly heights are wildly in error.

4.2. Test 2: Inversion of Rayleigh Wave Data With General Oxide Geochemistry Constraints

The second test was also using only the Rayleigh wave dispersion data, but applying constraints on the bounds of the oxide chemistries as given in Table 3 for the lithospheric mantle, and Table 4 for the sublithospheric mantle. For this test, a total of 9866 models were retained as a representative sample of the posterior PDFs, of which 3332 models had an nRMS $\leq$ 1.00 (yellow), 2467 an nRMS $\leq$ 0.89 (red), and 494 an nRMS $\leq$ 0.60 (blue).

Figures SI2.1–SI2.5 in the supporting information plot the same information as Figures 2–10 for Test 1. The Rayleigh wave dispersion data are fit to within their errors (supporting information Figure SI2.1A), as before, with reasonable models (supporting information Figure SI2.2), but now the oxide chemistries of the lithospheric and sublithospheric layers are within acceptable bounds (supporting information Figure SI2.3), as

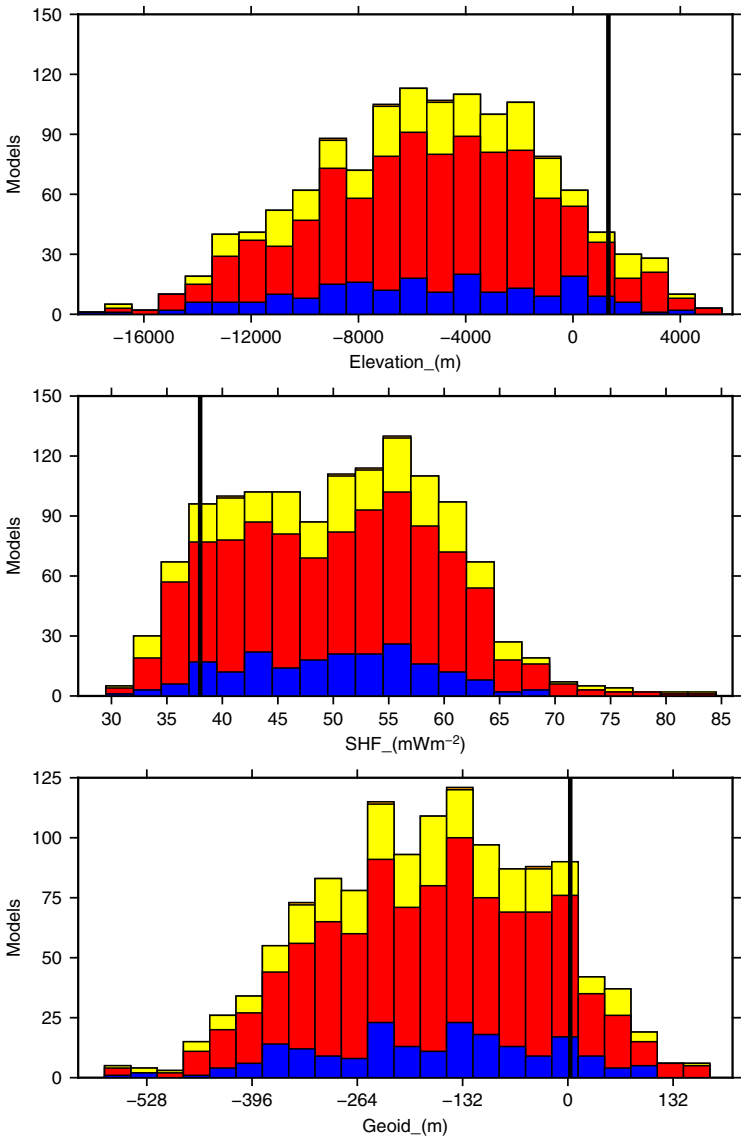

Figure 10. (top) Posterior PDFs of the elevation, (middle) surface heat flow, and (bottom) geoid height corresponding to Test 1. Yellow denotes models with an nRMS ≤ 1, red nRMS ≤ 0.93, and blue nRMS ≤ 0.60. The solid vertical black lines are the actual observations

prescribed. The posterior LAB now is bounded from ~140 to 350 km (supporting information Figures SI2.1B and SI2.4)—all of the models from Test 1 with shallower lithospheres are no longer acceptable, and even those with LAB depths of ~140 km are outside the 1σ error bounds for significant portions of the dispersion curve (supporting information Figure SI2.2) so would fail run tests of the residuals, such as the Durbin-Watson statistic [*Durbin and Watson*, 1971].

These models also yield implausible elevations and geoid heights that are wildly in error of observation (supporting information Figure SI2.5), and are thus not acceptable.

4.3. Test 3: Inversion of Rayleigh Wave Data, Filtered Geoid Height, and Surface Heat Flow Data With General Oxide Geochemistry Constraints

In the third test in this series, models were sought that fit not only the Rayleigh wave dispersion data, but that also were consistent, within statistical limits, with the filtered geoid height data and the surface heat flow data. Prior oxide distributions were uniform within the limits given in Tables 3 and 4. From the 200,000 candidate models, a total of 8449 were retained as a representative sample of the posterior PDFs, of which 6325 models had an nRMS ≤ 1.00 (yellow), 2113 an nRMS ≤ 0.66 (red), 423 an nRMS ≤ 0.46 (blue), and 1667

had an nRMS $<$ 1.00 (gold) for each of the three data types individually. Often when performing joint inversion of multiple data types, one data type can be overfit (low nRMS) and another data type underfit (high nRMS), but with an aggregate nRMS that it acceptable. These gold models are acceptable independently to all three data types simultaneously, so there is no trade-off of one data type against another.

The models are plotted in supporting information Figures SI3.1–SI3.5 for the same plots as for the first two tests. The data are fit to within their errors (supporting information Figure SI3.1A), as before, with reasonable velocity models (supporting information Figure SI3.2), and with oxide chemistries of the lithospheric and sublithospheric layers within acceptable bounds (supporting information Figure SI3.3), again as prescribed. The posterior LAB now is bounded from $>$150 to $<$340 km (supporting information Figures SI3.1B and SI3.4)—all of the models with shallow lithospheres are no longer acceptable; even those close to the upper and lower bounds could be considered unacceptable based on the serial correlations of the residuals of their fit to the Rayleigh wave data.

These models also fit the geoid and SHF observations (supporting information Figure SI3.5), as required. They predict elevations with a posterior distribution shown in supporting information Figure SI3.5, with the gold models giving a mean and median at $-$415 m and $-$393 m, respectively, with one sigma sample standard deviation of the distribution of $\pm$500 m and 95% confidence limits of the mean of $\pm$25 m. Without further analysis or inclusion of more data, this would be our final conclusion.

4.4. Test 4: Inversion of Rayleigh Wave Data, Filtered Geoid Height and Surface Heat Flow Data Plus MT Data With General Oxide Geochemistry Constraints

In the fourth test, models are sought that fit the MT data as well as the other three data types, namely Rayleigh wave data, filtered geoid height data and surface heat flow data. However, it is impossible to fit the MT data with a single-layered lithosphere, i.e., a layer of constant water content with conductivity varying only as a function of increasing temperature and iron content. There must be water content variation with depth, and tests demonstrated that a minimum of three layers is required to satisfy the MT data.

A three-layered lithosphere is also supported by the geochemical oxide layering of the Kaapvaal lithosphere and sublithospheric mantle (asthenosphere) based on *Griffin et al*. [2003] (see Table 5). Also, a recent *S* wave receive function study found distinctive layering of the Kaapvaal lithosphere, with three layers exhibiting different behavior [*Sodoudi et al*., 2013]. The uniform prior distributions of the lithospheric layers were 70–120 km for MLD1 (first mid-lithospheric discontinuity), 140–190 for MLD2, and 200–350 for the LAB. Lithospheric layering was also identified below the composite Kalahari Craton by *Wittlinger and Farra* [2007], with seismic conversions at the same depth ranges as identified by *Sodoudi et al*. [2013].

In this fourth test, there were no constraints imposed on the water content within the lithospheric layers except for requiring $<$1000 wt ppm bulk water, nor on the oxide distributions within each lithospheric layer except that they were bounded by the ranges given in Tables 3 and 4.

The parameter space for a three-layer lithosphere is increased to 41 parameters, from 29 parameters for a single-layered lithosphere, by the addition of

1. Two parameters for the water content in the additional two lithospheric layers.
2. Eight parameters related to the four oxides in the additional two lithospheric layers.
3. Two parameters for the permitted depth variation of the mid-lithospheric discontinuities

When only 200,000 candidate models were generated, as per the three prior trials, of the 8716 that made up the final posterior PDFs only 138 models had an nRMS $\leq$ 1.00 and only 8 models had an nRMS $<$ 1.00 for each data type individually. This demonstrated that when MT data are included there has to be a far greater number of models generated and tested given the increase in the number of parameters and the sensitivity of MT data to variations in temperature and water content. Thus, to more fully explore the 41 parameter model space, five million candidate models were generated in the second run of this trial, with adaptation of the prior distributions every 500,000 models. A total of 310 models with total nRMS $<$ 1.00 (yellow) were found, of which four have an nRMS $<$ 1 (gold) for each of the four data types individually.

All four data types are clearly well fit within their errors (supporting information Figures SI4.1A, SI4.5, and SI4.7).

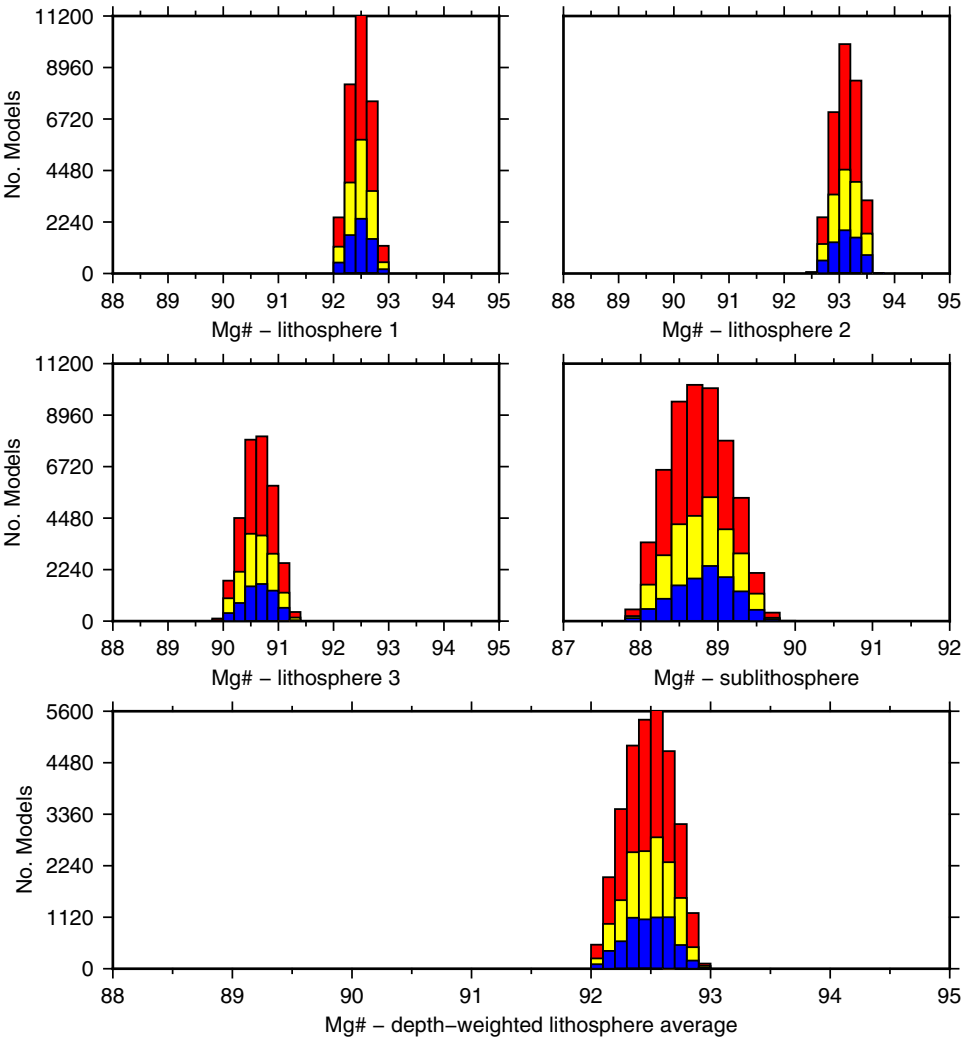

Figure 11. Posterior PDFs of the Mg# within the three lithospheric layers (top left, top right, and middle left) and the sublithospheric mantle (middle right) layer (column 4) corresponding to our preferred model. Red denotes models that fit data with a normalized summed RMS of <1.09, yellow denotes models with an nRMS < 1.00, and blue denotes models with an nRMS < 0.92.

The MT data do not allow LABs shallower than 200 km, as concluded by *Fullea et al*. [2011] in their forward modeling of the MT data from site KIM015. The posterior PDFs infer an LAB around 260–280 km (supporting information Figure SI4.5), and an elevation around −600 to −300 m (supporting information Figure SI4.6).

Although these models fit the four data types, they are not consistent with other information.

1. The geotherms from these successful models (supporting information Figure SI4.6) exhibit a steeper gradient in the shallower parts and a lower gradient in the deeper parts than the standard geotherm "K2" for the Kaapvaal Craton [*Jones*, 1988] and P-T estimates derived by geothermobarometric analyses of xenolith samples from the kimberlitic eruptions at Jagersfontein as given in *James et al*. [2004], *Woodland and Koch* [2003], *Peslier et al*. [2010], and *Baptiste and Tommasi* [2014]. Within this context, however, we have to emphasize that the geotherms derived from xenoliths are not directly comparable to those obtained by our inversion. Xenolith-derived geotherms are representative of the thermal state of the mantle at the time of xenolith extrusion, whereas geotherms obtained by inverting present-day data sets are representative of present day thermal state. With these considerations, it is perhaps not surprising then that the geotherms from our inversion are compatible with slightly deeper LAB, as they are expected to represent a relaxed thermal state compared to that at the time of volcanism.

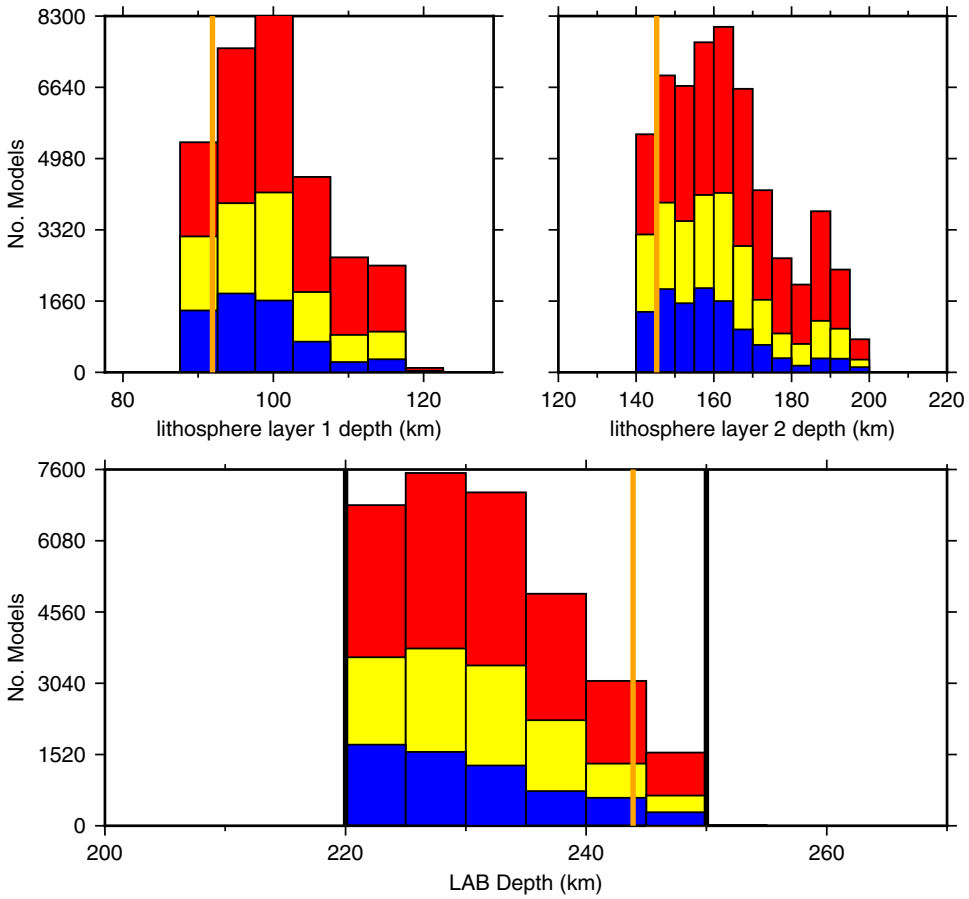

Figure 12. Posterior PDFs of lithospheric mantle interface depths, (top left) MLD1, (top right) MLD2, and (bottom) LAB corresponding to our preferred models. Red denotes models that fit data with a normalized summed RMS of <1.09, yellow denotes models with an nRMS < 1.00, and blue denotes models with an nRMS, 0.92. The prior PDFs for the interfaces had bounds of 70–120 km for MLD1, 140–200 km for MLD2, and 220–250 km for the LAB (bounds denoted by solid vertical black lines). The solid vertical gold lines on each plot indicate the interface depths of the best fitting model, with an nRMS of 0.60.

2. The oxide geochemistry in each of the lithospheric layers does not exhibit the stratification observed in xenoliths from the Kaapvaal Craton as listed in Table 5 with a Low-T lherzolitic upper lithospheric mantle layer overlying a far more depleted harzburgitic layer below with is a relatively fertile High-T lherzolitic basal lithospheric mantle layer.
3. The water contents in the MT models are far too extreme in the upper lithospheric layer and well beyond the notional 180 wt ppm H_2O bulk water permissible in Nominally Anhydrous Minerals (NAMs) in residual lherzolite in the lithospheric mantle [*Green et al*., 2010, 2011].

4.5. Test 5: Inversion of Rayleigh Wave Data, Filtered Geoid Height, and Surface Heat Flow Data Plus MT Data With Layer-Specific Oxide Geochemistry Constraints and Consistent With Geotherm and Water Content

As we show above in Test 4, we can fit all of the data satisfactorily with a three-layered lithosphere allowing for only general bounds on the oxide chemistry of the layers (Table 3, taken from *Afonso et al*. [2008]) and on the water contents within each layer [see *Peslier et al*., 2010]. In the successful models there was though little difference in oxide chemistry between the three mantle lithospheric layers, demonstrating that these surface geophysical observations cannot uniquely define the oxide chemistry of individual lithospheric layers, only the average composition of the whole lithosphere.

This lack of distinctiveness in the oxide chemistry of the lithospheric layers is inconsistent with observations from xenoliths [*Griffin et al*., 2003], so in the final refinement we constrain the oxide chemistry of the layers to be chosen from prior distributions consistent with the known chemical layering defined by analyzing

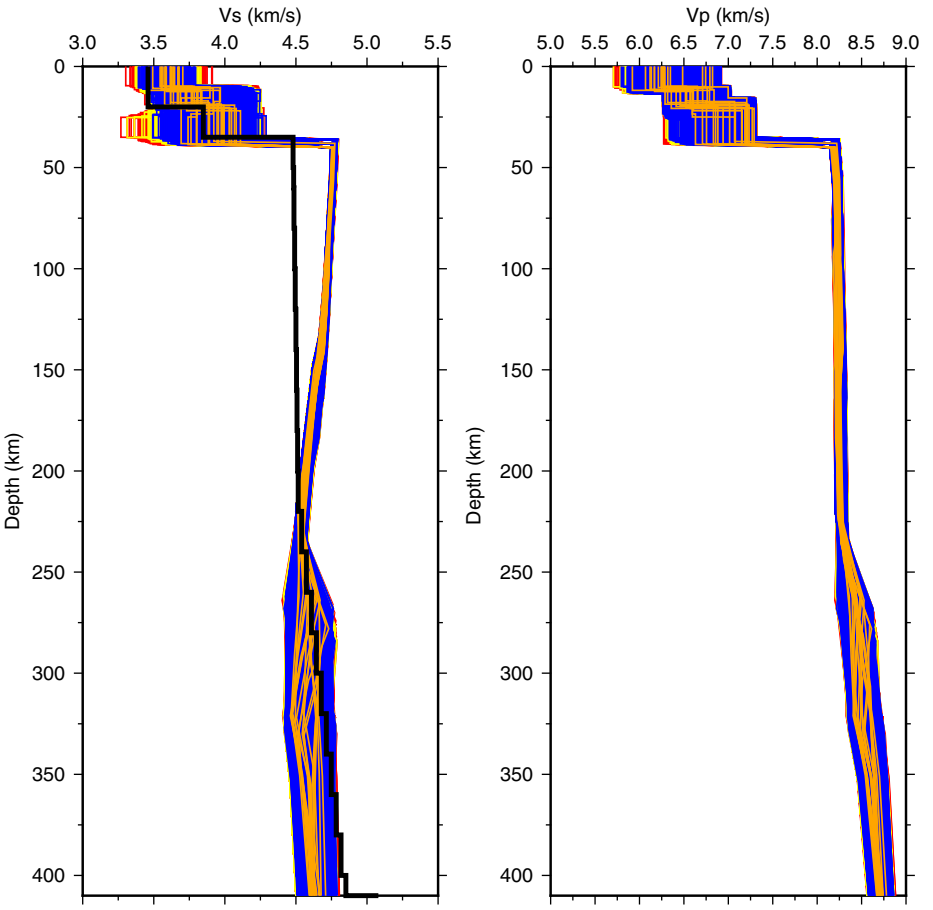

Figure 13. Seismic models corresponding to Test 5. (a) Seismic Vs (left column) and Vp (right column) models. Also plotted on the Vs models figure is the standard AK135 spherically averaged model of *Kennett et al*. [1995]. Note that lithospheric velocities are all greater than AK135, which is to be expected for a craton.

xenoliths exhumed in the Group I kimberlite pipes that pepper the Kaapvaal Craton (Table 5) [*Griffin et al*., 2003], and require the depth variation in water content to be consistent with xenolith observations [*Peslier et al*., 2010]. Each of the sublithospheric mantle layers was assigned a range of oxide composition based on these observations, and the sublithospheric mantle an initial oxide chemistry based on a ranges for Primitive Upper Mantle from *McDonough and Sun* [1995] and *Lyubetskaya and Korenaga* [2007] (Table 4). Finally, both the geotherms from heat flow models [*Jones*, 1988] and from P-T estimates from geothermobarometry [*Woodland and Koch*, 2003] on the xenolith samples infer a lithosphere-asthenosphere boundary (LAB) in the range of 220–250 km, so this depth range constraint was applied in order to yield models consistent with those data.

Thus, in this final Test 5 the four data types were again inverted but ensuring that prior PDFs honored observed xenolith geochemical stratigraphy (Table 5), that the modeled the geotherms were consistent with the Kaapvaal Craton geotherm (K2, *Jones* [1988]) and with P-T geothermobarometric estimates [*James et al*., 2004; *Woodland and Koch*, 2003; *Peslier et al*., 2010; *Baptiste and Tommasi*, 2014] by setting the prior PDF for the LAB to 220–250 km, and that the water contents were consistent with those observed [*Peslier et al*., 2010; *Baptiste et al*., 2012]. A total of 10 independent runs were performed simultaneously to fully explore model space. Each run sampled 30 million thermochemical lithospheric models and tested them against observations. Of the 300 million candidate models tested, we found 15,000 models that fit the four data types to an average nRMS < 1. The histogram of the nRMS misfits of all of best final models are shown in supporting information Figure SI5.1, together with the fits to the Rayleigh dispersion data and the MT data (supporting information Figures SI5.2 and SI5.3).

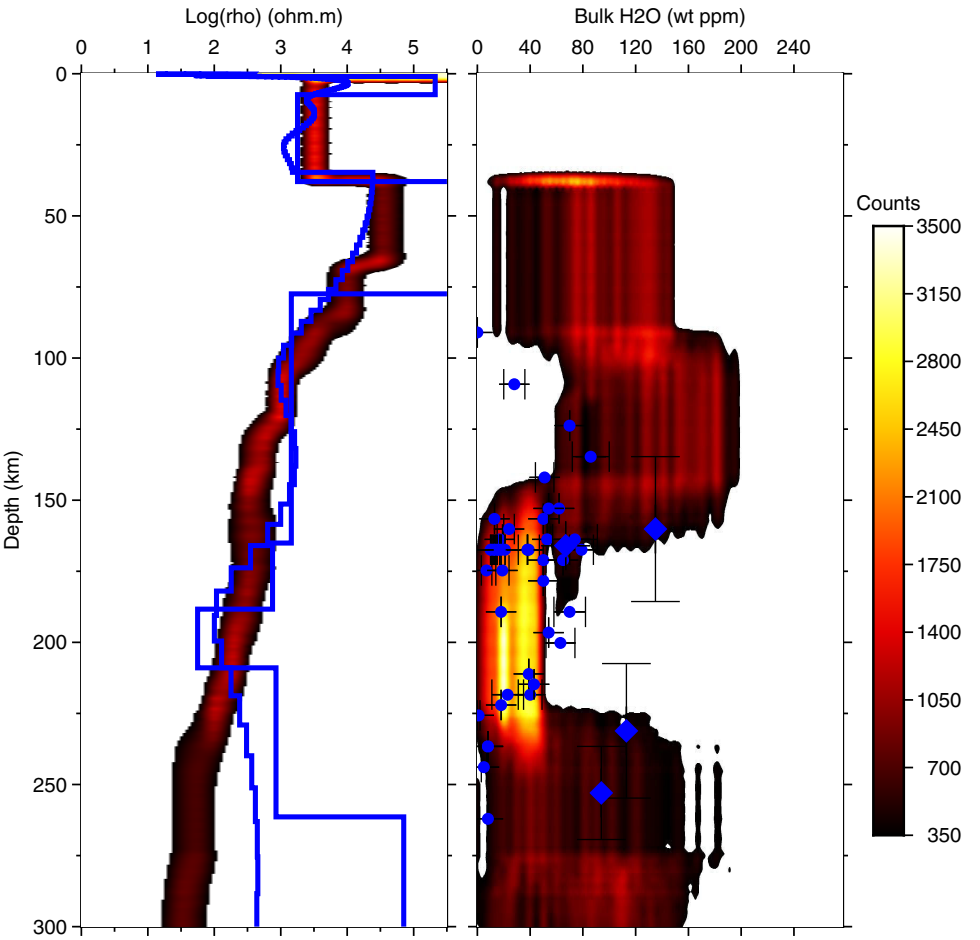

Figure 14. (left column) Electrical resistivity and (right column) bulk water content 2-D histograms corresponding to Test 5. Also shown on the resistivity models plot are the best fitting layered Earth models and best fitting Occam smooth model (black lines). The water models plot include the bulk water and water in olivine contents from *Peslier et al.* [2010] as blue symbols with error bounds.

The final posterior PDFs of Mg# (Figure 11) are consistent with a highly depleted uppermost and middle lithosphere (Mg# $>$ 92.5, Figure 11), and a relatively fertile (for cratonic lithosphere) lower lithosphere mantle (Mg# $=$ 90.5, Figure 11, middle row left), which results in a depleted lithospheric average of Mg# $=$ 92.75–93.0 (Figure 11, bottom). The sublithospheric mantle has a more fertile composition with Mg# $=$ 87.75–88.25 (Figure 11, middle row right).

Figure 12 shows the posterior PDFs of the mid-lithospheric discontinuities' depths (MLDs) and the depth of the lithosphere-asthenosphere boundary (LAB). The prior bounds for MLD depths were prescribed to be consistent with the geochemical layering inferred from abundant xenolith evidence [*Griffin et al.*, 1999, 2003]. The final models all have tight depth ranges for the MLD boundaries at 95–105 km and 160–165 km, respectively.

The median LAB for nRMS $<$ 1 models is 230 $\pm$ 7 km (Figure 12, bottom). The depth to the LAB beneath the Kaapvaal Craton has been estimated using a variety of body wave, surface waves and receiver function seismic methods (Table 1 of *James et al.* [2001]), yielding interpreted estimates from 140 to 370 km. As with the global analysis of P-to-S converted phases (P receiver functions) by *Rychert and Shearer* [2009], who suggested that an imaged interface at 95 $\pm$ 4 km beneath Precambrian regions could not possibly constitute the LAB, any LAB estimate that is shallower than the approx. 160 km graphite-diamond stability field below cratons [*Kennedy and Kennedy*, 1976], plus a "diamond window" of the order of 30 km, is clearly difficult to justify for cratonic regions that have recent diamond-hosting kimberlites and fast seismic velocities. Our LAB estimate of 230 $\pm$ 7 km compares well with the LAB defined on the basis of petrological modeling of

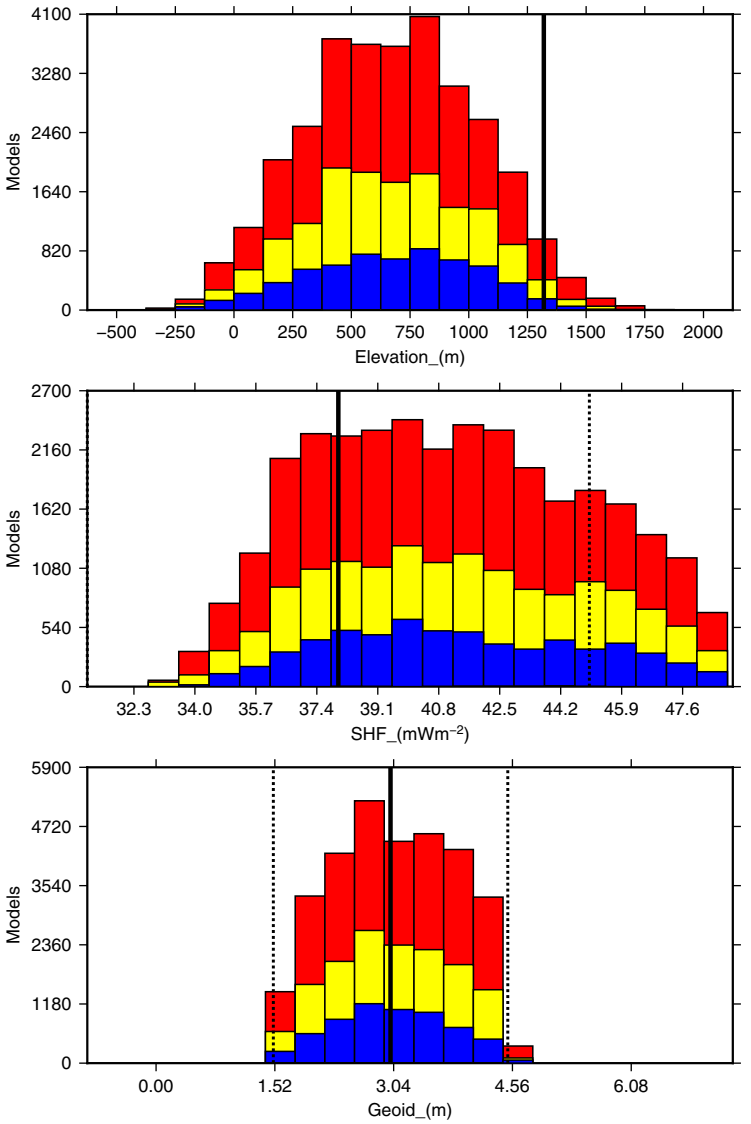

Figure 15. (top) Posterior PDFs of the predicted elevation, (middle) surface heat flow, and (bottom) geoid. Only models that fit within the statistical bounds of the SHF and geoid were accepted. The solid vertical black line on each plot denotes the data value, and the dashed vertical black lines the standard errors of the mean values. Red denotes models that fit with a normalized summed RMS of $<$1.09, yellow denotes models with an nRMS $<$ 1.00, and blue denotes models with an nRMS $<$ 0.92.

MT data by *Fullea et al*. [2011] (230–260 km), and is close to LAB depth estimates defined on the basis of S receiver functions by *Sodoudi et al*. [2013] (260–280 km) and on 1-D SH velocity modeling of SASE data by *Brandt et al*. [2012] (220 km). However, our results are considerably deeper than the 180–200 km estimate from the surface wave tomographic model of *Fishwick* [2010].

The Vp and Vs seismic models and the electrical resistivity and water content models are shown in Figures 13 and 14, respectively. From the acceptable velocity models, we find high Vs in the uppermost lithosphere (4.8 km/s) that decreases progressively with depth to a minimum of 4.5 km/s at 275 km. At all lithospheric depths Vs is greater than the global average AK135 (black line, Figure 13a, left), which is hardly surprising given the cratonic nature of the lithosphere. In contrast, the Vp models exhibit a relatively uniform velocity of around 8.25 km/s for the whole of the lithospheric mantle. Note that the MT models derived from MT data alone (solid blue lines, Figure 14a) are reasonably consistent with those petrologically supported, except for the asthenosphere where our models yield low resistivities whereas the unconstrained MT models (blue lines, Figure 14a, left) suggest thermally implausibly high resistivities. From the water models

(Figure 14a, right), consistent with the observations of *Peslier et al*. [2010], we find a drier upper lithosphere and a wetter middle lithosphere; these layers were free to take values in the range of 0–200 wt ppm. The lower lithosphere was constrained to be no greater than 50 wt ppm, based on *Peslier et al*. [2010].

These best fitting models yield elevation, SHF, and geoid height posterior distributions shown in Figure 15. The SHF and geoid anomalies all fit within the prescribed limits, as required. Elevation was set as a free parameter and therefore it represents the elevation accounting for the thermochemical lithospheric models that successfully fit the constraining data sets. The best fitting 15,000 models, of the 300 million candidate models tested, with total nRMS < 1 (yellow) to the filtered geoid, SHF, Rayleigh dispersion data and MT data yield a posterior elevation PDF with a mean and median of 668 m, standard sample deviation of 320 m, and 95% confidence interval of the mean of ± 3 m. The distribution has zero skewness (symmetric distribution) but a small negative kurtosis (-0.8), indicative of a slightly flatter distribution than Gaussian.

We thus conclude that the lithosphere beneath the Jagersfontein kimberlite field can isostatically support an elevation of the order of 670 m. The observed regional average elevation of 1320 m thus requires some 650 m of sublithospheric dynamic topographic support.

5. Conclusions

Taking advantage of the high-quality geophysical and geochemical information available on different aspects of the lithospheric structure beneath southern Africa, we constrain the amount of dynamic topographic support in this region by performing constrained joint inversions of four distinct and complementary data types. Our analysis is based on a Monte Carlo stochastic hypothesis testing approach, using the geoid anomaly, surface-wave dispersion data, magnetotelluric data, and surface heat flow measurements. We undertook a series of tests of progressively increasing data complexity and constraint complexity, finally using all four data sets with geochemical, thermal and water content constraints as given by reliable, independent observations.

Our overarching conclusion is that the lithosphere beneath the Jagersfontein kimberlite field can isostatically support ~670 m of elevation due to its own thermochemical structure. This suggests that dynamic support from below the lithosphere must account for ~650 m of the current regional average elevation of 1320 m. This value is reasonably consistent with the long-standing estimate of 500 m of *Nyblade and Robinson* [1994], which was based on simpler arguments but that has withstood the test of time, and consistent with the 500 m estimate for long wavelength mantle anomalies by *Hoggard et al*. [2016].

All of the data types were required to undertake this derivation. The thermal structure was mainly controlled by the SHF, surface wave (SW) and MT data, and the density structure by the geoid height data, xenolith information and, to a lesser extent, by the SW data. When no constrains on plausible compositions for the lithosphere are imposed, sensitivity to the thermal structure of the lithosphere and the LAB, which control isostatic topography [see, e.g., *Jones et al*., 2014], came primarily from the MT data, as the available SW data alone permits a wide range for LAB depths (Test 1). The lithospheric layering was prescribed by the MT data alone and is consistent with observed chemical and seismological layering; the three other data types accept a single layer lithosphere. In summary, it is the combination of complementary data sets, with additional constrains on realistic compositional structures from xenoliths, that allows us to obtain a detailed lithospheric model and precise estimates of isostatic (lithospheric) and dynamic topography of the Southern African Plateau. We agree with *Flament et al*. [2013] that constraining present-day dynamic topography can only be achieved with detailed knowledge of the thermochemical structure of the lithosphere. The results from this study thus provide a "benchmark point" for calibrating global models of dynamic topography.

Acknowledgments
The authors thank all those on the Southern African MT Experiment (SAMTEX) listed in the acknowledgements of *Jones et al*. [2009]. Joanne Adam is thanked for providing the digital files for the dispersion curves for the Kaapvaal Craton from *Adam and Lebedev* [2012]. The authors thank the reviewer and the editor for their constructive comments that improved our presentation of this work. All of the data discussed herein are available in the public domain. The elevation data are taken from ETOPO1, and the geoid data from EGM2008 [*Pavlis et al*., 2012]. The heat flow data are presented in *Jones* [1988], the Rayleigh wave dispersion data in *Adam and Lebedev* [2012], and the MT data in *Jones et al*. [2013]. The work of JCA has been supported by two ARC DP projects (DP120102372, DP160103502). AGJ was supported in two month-long visits to Macquarie University through Science Foundation Ireland grants (IRETHERM: 10/IN.1/I3022 and 10/IN.1/I3022-STTF 11). JF was funded by the People Programme (Marie Curie Actions) of the European Union's H2020-MSCA-IF-2014 program under REA grant 657357, and Science Foundation Ireland grant 16/ERCD/4303. All of the plots were made using GMT, and Paul Wessel and colleagues [*Wessel et al*., 2013] are thanked for their huge contribution in making GMT available to the community.

References

Adam, J. M. C., and S. Lebedev (2012), Azimuthal anisotropy beneath southern Africa from very broad-band surface-wave dispersion measurements, *Geophys. J. Int.*, *191*(1), 155–174.

Afonso, J. C. (2006), *Thermal, Density, Seismological, and Rheological Structure of the Lithospheric-Sublithospheric Mantle From Combined Petrological-Geophysical Modelling: Insights on Lithospheric Stability and the Initiation of Subduction*, Carleton Univ., Ottawa, Canada.

Afonso, J. C., M. Fernandez, G. Ranalli, W. L. Griffin, and J. A. D. Connolly (2008), Integrated geophysical-petrological modeling of the lithosphere and sublithospheric upper mantle: Methodology and applications, *Geochem. Geophys. Geosyst.*, *9*, Q05008, doi:10.1029/2007GC001834.

Afonso, J. C., J. Fullea, Y. Yang, J. A. D. Connolly, and A. G. Jones (2013a), 3-D multi-observable probabilistic inversion for the compositional and thermal structure of the lithosphere and upper mantle. II: General methodology and resolution analysis, *J. Geophys. Res. Solid Earth*, *118*, 1650–1676, doi:10.1002/jgrb.50123.

Afonso, J. C., J. Fullea, W. L. Griffin, Y. Yang, A. G. Jones, J. A. D. Connolly, and S. Y. O'Reilly (2013b), 3-D multiobservable probabilistic inversion for the compositional and thermal structure of the lithosphere and upper mantle. I: A priori petrological information and geophysical observables, *J. Geophys. Res. Solid Earth*, *118*, 2586–2617, doi:10.1002/jgrb.50124.

Afonso, J. C., M. Mookamp, and J. Fullea (2016a), Imaging the lithosphere and upper mantle: Where we are at and where we are going, in *Integrated Imaging of the Earth, Theory and Applications*, edited by M. Moorkamp et al., pp. 191–218, AGU, Washington, D. C.

Afonso, J. C., N. Rawlinson, Y. Yang, D. L. Schutt, A. G. Jones, J. Fullea, and W. L. Griffin (2016b), 3D multi-observable probabilistic inversion for the compositional and thermal structure of the lithosphere and upper mantle. III: Thermochemical Tomography in the Western-Central US, *J. Geophys. Res. Solid Earth*, *121*, 7337–7370, doi:10.1002/2016JB13049.

Baptiste, V., and A. Tommasi (2014), Petrophysical constraints on the seismic properties of the Kaapvaal craton mantle root, *Solid Earth*, *5*(1), 45–63.

Baptiste, V., A. Tommasi, and S. Demouchy (2012), Deformation and hydration of the lithospheric mantle beneath the Kaapvaal craton, South Africa, *Lithos*, *149*, 31–50.

Bowin, C. (2000), Mass anomaly structure of the Earth, *Rev. Geophys.*, *38*(3), 355–387.

Brandt, M. B. C., S. P. Grand, A. A. Nyblade, and P. H. G. M. Dirks (2012), Upper mantle seismic structure beneath Southern Africa: Constraints on the buoyancy supporting the African superswell, *Pure Appl. Geophys.*, *169*(4), 595–614.

Christensen, N., and W. Mooney (1995), Seismic velocity structure and composition of the continental crust: A global view, *J. Geophys. Res.*, *100*(B6), 9761–9788.

Colli, L., S. Ghelichkhan, and H. P. Bunge (2016), On the ratio of dynamic topography and gravity anomalies in a dynamic Earth, *Geophys. Res. Lett.*, *43*, 2510–2516, doi:10.1002/2016GL067929.

Connolly, J. A. D. (2009), The geodynamic equation of state: What and how, *Geochem. Geophys. Geosyst.*, *10*, Q10014, doi:10.1029/2009GC002540.

Durbin, J., and G. S. Watson (1971), Testing for serial correlation in least squares regression, *Biometrika*, *58*(1), 1–19.

Fishwick, S. (2010), Surface wave tomography: Imaging of the lithosphere-asthenosphere boundary beneath central and southern Africa?, *Lithos*, *120*(1–2), 63–73.

Flament, N., M. Gurnis, and R. D. Muller (2013), A review of observations and models of dynamic topography, *Lithosphere*, *5*(2), 189–210.

Fullea, J., M. R. Muller, and A. G. Jones (2011), Electrical conductivity of continental lithospheric mantle from integrated geophysical and petrological modeling: Application to the Kaapvaal Craton and Rehoboth Terrane, southern Africa, *J. Geophys. Res.*, *116*, B10202, doi:10.1029/2011JB008544.

Green, D. H., W. O. Hibberson, I. Kovacs, and A. Rosenthal (2010), Water and its influence on the lithosphere-asthenosphere boundary, *Nature*, *467*(7314), 448–451.

Green, D. H., W. O. Hibberson, I. Kovacs, and A. Rosenthal (2011), Water and its influence on the lithosphere-asthenosphere boundary, *Nature*, *472*(7344), 504–504.

Griffin, W. L., S. Y. O'Reilly, and C. G. Ryan (1999), The composition and origin of sub-continental lithospheric mantle, in *Mantle Petrology: Field Observations and High-Pressure Experimentation: A Tribute to Francis R. (Joe) Boyd*, edited by Y. Fei, C. M. Berkta and B. O. Mysen, vol. 6, pp. 13–45, Spec. Publ. Geochem. Soc., Washington, D. C.

Griffin, W. L., S. Y. O'Reilly, L. M. Natapov, and C. G. Ryan (2003), The evolution of lithospheric mantle beneath the Kalahari Craton and its margins, *Lithos*, *71*(2–4), 215–241.

Gurnis, M., J. X. Mitrovica, J. Ritsema, and H.-J. van Heijst (2000), Constraining mantle density structure using geological evidence of surface uplift rates: The case of the African Superplume, *Geochem. Geophys. Geosyst.*, *1*(7), 1020, doi:10.1029/1999GC000035.

Haario, H., M. Laine, A. Mira, and E. Saksman (2006), DRAM: Efficient adaptive MCMC, *Stat. Comput.*, *16*(4), 339–354.

Hager, B. H., R. W. Clayton, M. A. Richards, R. P. Comer, and A. M. Dziewonski (1985), Lower mantle heterogeneity, dynamic topography and the geoid, *Nature*, *313*(6003), 541–546.

Hoggard, M. J., N. White, and D. Al-Attar (2016), Global dynamic topography observations reveal limited influence of large-scale mantle flow, *Nat. Geosci.*, *9*(6), 456–463.

James, D. E., M. J. Fouch, J. C. VanDecar, and S. van der Lee (2001), Tectospheric structure beneath southern Africa, *Geophys. Res. Lett.*, *28*(13), 2485–2488.

James, D. E., F. L. Niu, and J. Rokosky (2003), Crustal structure of the Kaapvaal craton and its significance for early crustal evolution, *Lithos*, *71*(2–4), 413–429.

James, D. E., F. R. Boyd, D. Schutt, D. R. Bell, and R. W. Carlson (2004), Xenolith constraints on seismic velocities in the upper mantle beneath southern Africa, *Geochem. Geophys. Geosyst.*, *5*, Q01002, doi: 10.1029/2003GC000551.

Jones, A. G. (1982), On the electrical crust-mantle structure in Fennoscandia: No Moho and the asthenosphere revealed?, *Geophys. J. R. Astron. Soc.*, *68*(2), 371–388.

Jones, A. G. (1999), Imaging the continental upper mantle using electromagnetic methods, *Lithos*, *48*(1–4), 57–80.

Jones, A. G. (2012), Distortion decomposition of the magnetotelluric impedance tensors from a one-dimensional anisotropic Earth, *Geophys. J. Int.*, *189*(1), 268–284.

Jones, A. G., R. L. Evans, and D. W. Eaton (2009), Velocity-conductivity relationships for mantle mineral assemblages in Archean cratonic lithosphere based on a review of laboratory data and Hashin-Shtrikman extremal bounds, *Lithos*, *109*(1–2), 131–143, doi:10.1016/j.lithos.2008.10.014.

Jones, A. G., M. R. Muller, S. Fishwick, R. L. Evans, and J. Fullea (2013), Velocity-conductivity relations for cratonic lithosphere and their application: Example of Southern Africa, *Geochem. Geophys. Geosyst.*, *14*, 806–827, doi:10.1002/ggge.20075.

Jones, A. G., J. C. Afonso, J. Fullea, and F. Salajegheh (2014), The lithosphere-asthenosphere system beneath Ireland from integrated geophysical-petrological modeling—I: Observations, 1D and 2D hypothesis testing and modeling, *Lithos*, *189*, 28–48, doi: 10.1016/j.lithos.2013.10.033.

Jones, M. Q. W. (1988), Heat flow in the Witwatersrand Basin and environs and its significance for the South African shield geotherm and lithosphere thickness, *J. Geophys. Res.*, *93*(B4), 3243–3260.

Jones, M. Q. W. (1998), A review of heat flow in southern Africa and the thermal structure of the lithosphere, *S. Afr. Geophys. Rev.*, *2*, 115–122.

Kennedy, C. S., and G. C. Kennedy (1976), Equilibrium boundary between graphite and diamond, *J. Geophys. Res.*, *81*(14), 2467–2470.

Kennett, B. L. N., E. R. Engdahl, and R. Buland (1995), Constraints on seismic velocities in the Earth from travel times, *Geophys. J. R. Astron. Soc.*, *122*, 108–124.

Kgaswane, E. M., A. A. Nyblade, J. Julia, P. Dirks, R. J. Durrheim, and M. E. Pasyanos (2009), Shear wave velocity structure of the lower crust in southern Africa: Evidence for compositional heterogeneity within Archaean and Proterozoic terrains, *J. Geophys. Res.*, *114*, B12304, doi:10.1029/2008JB006217.

Lebedev, S., J. Boonen, and J. Trampert (2009), Seismic structure of Precambrian lithosphere: New constraints from broad-band surface-wave dispersion, *Lithos*, *109*(1–2), 96–111.

Lithgow-Bertelloni, C., and P. G. Silver (1998), Dynamic topography, plate driving forces and the African superswell, *Nature*, *395*(6699), 269–272.

Lyubetskaya, T., and J. Korenaga (2007), Chemical composition of Earth's primitive mantle and its variance: 1. Method and results, *J. Geophys. Res.*, *112*, B03211, doi:10.1029/2005JB004223.

McDonough, W. F., and S. S. Sun (1995), The composition of the Earth, *Chem. Geol.*, *120*(3–4), 223–253.

McKenzie, D., and M. J. Bickle (1988), The volume and composition of melt generated by extension of the lithosphere, *J. Petrol.*, *29*(3), 625–679.

McKenzie, D., and M. J. Bickle (1990), A eutectic parameterization of mantle melting, *J. Phys. Earth*, *38*(6), 511–515.

Muller, M. R., J. Fullea, A. G. Jones, J. Adam, S. Lebedev, and N. P. Agostinetti (2013), Lithospheric-Mantle structure of the Kaapvaal Craton, South Africa, derived from thermodynamically self-consistent modelling of magnetotelluric, surface-wave dispersion, S-wave receiver function, heat-flow, elevation and xenolith observations, in *European Geoscience Union General Assembly 2013*, Eur. Geosci. Union, Vienna, Austria, Geophysical Research Abstracts EGU2013-12903.

Nguuri, T. K., J. Gore, D. E. James, S. J. Webb, C. Wright, T. G. Zengeni, O. Gwavava, J. A. Snoke, and G. Kaapvaal Seismic (2001), Crustal structure beneath southern Africa and its implications for the formation and evolution of the Kaapvaal and Zimbabwe cratons, *Geophys. Res. Lett.*, *28*(13), 2501–2504.

Nyblade, A. A., and S. W. Robinson (1994), The African Superswell, *Geophys. Res. Lett.*, *21*(9), 765–768.

Parker, R. L., and J. R. Booker (1996), Optimal one-dimensional inversion and bounding of magnetotelluric apparent resistivity and phase measurements, *Phys. Earth Planet. Inter.*, *98*(3–4), 269–282.

Pavlenkova, N. I., G. A. Pavlenkova, and L. N. Solodilov (1996), High velocities in the uppermost mantle of the Siberian craton, *Tectonophysics*, *262*(1–4), 51–65.

Pavlis, N. K., S. A. Holmes, S. C. Kenyon, and J. K. Factor (2012), The development and evaluation of the Earth Gravitational Model 2008 (EGM2008), *J. Geophys. Res.*, *117*, B04406, doi:10.1029/2011JB008916.

Peslier, A. H., A. B. Woodland, D. R. Bell, and M. Lazarov (2010), Olivine water contents in the continental lithosphere and the longevity of cratons, *Nature*, *467*(7311), 78–81.

Romanowicz, B., and Y. C. Gung (2002), Superplumes from the core-mantle boundary to the lithosphere: Implications for heat flux, *Science*, *296*(5567), 513–516.

Rychert, C. A., and P. M. Shearer (2009), A global view of the lithosphere-asthenosphere boundary, *Science*, *324*(5926), 495–498.

Sodoudi, F., X. H. Yuan, R. Kind, S. Lebedev, J. M. C. Adam, E. Kastle, and F. Tilmann (2013), Seismic evidence for stratification in composition and anisotropic fabric within the thick lithosphere of Kalahari Craton, *Geochem. Geophys. Geosyst.*, *14*, 5393–5412, doi:10.1002/2013GC004955.

Stankiewicz, J., S. Chevrot, R. D. van der Hilst, and M. J. de Wit (2002), Crustal thickness, discontinuity depth, and upper mantle structure beneath southern Africa: constraints from body wave conversions, *Phys. Earth Planet. Inter.*, *130*(3–4), 235–251.

Steinberger, B. (2016), Topography caused by mantle density variations: observation-based estimates and models derived from tomography and lithosphere thickness, *Geophys. J. Int.*, *205*, 604–621.

Stixrude, L., and C. Lithgow-Bertelloni (2011), Thermodynamics of mantle minerals—II. Phase equilibria, *Geophys. J. Int.*, *184*(3), 1180–1213.

Vinnik, L. P., R. W. E. Green, L. O. Nicolaysen, G. L. Kosarev, and N. V. Petersen (1996), Deep seismic structure of the Kaapvaal craton, *Tectonophysics*, *262*(1–4), 67–75.

Wessel, P., W. H. F. Smith, R. Scharroo, J. F. Luis, and F. Wobbe (2013), Generic Mapping Tools: Improved version released, *EOS Trans. AGU*, *94*, 409–410.

Wittlinger, G., and V. Farra (2007), Converted waves reveal a thick and layered tectosphere beneath the Kalahari super-craton, *Earth Planet. Sci. Lett.*, *254*, 404–415.

Woodland, A. B., and M. Koch (2003), Variation in oxygen fugacity with depth in the upper mantle beneath the Kaapvaal craton, Southern Africa, *Earth Planet. Sci. Lett.*, *214*(1–2), 295–310.

Yang, Y., A. Li, and M. H. Ritzwoller (2008), Crustal and uppermost mantle structure in southern Africa revealed from ambient noise and teleseismic tomography, *Geophys. J. Int.*, *174*, 235–248.

Youssof, M., H. Thybo, I. M. Artemieva, and A. Levander (2013), Moho depth and crustal composition in Southern Africa, *Tectonophysics*, *609*, 267–287.